Understanding the Interface of Six-Shell Cuboctahedral and Icosahedral Palladium Clusters on Reduced Graphene Oxide: Experimental and Theoretical Study

Eduardo Gracia-Espino,[†,‡,§] Guangzhi Hu,[†,§] Andrey Shchukarev,[‡] and Thomas Wågberg*,[†]

[†]Department of Physics, Umeå University, 901 87 Umeå, Sweden
[‡]Department of Chemistry, Umeå University, 901 87 Umeå, Sweden

S *Supporting Information*

ABSTRACT: Studies on noble-metal-decorated carbon nano-structures are reported almost on a daily basis, but detailed studies on the nanoscale interactions for well-defined systems are very rare. Here we report a study of reduced graphene oxide (rGOx) homogeneously decorated with palladium (Pd) nanoclusters with well-defined shape and size (2.3 ± 0.3 nm). The rGOx was modified with benzyl mercaptan (BnSH) to improve the interaction with Pd clusters, and N,N-dimethylformamide was used as solvent and capping agent during the decoration process. The resulting Pd nanoparticles anchored to the rGOx-surface exhibit high crystallinity and are fully consistent with six-shell cuboctahedral and icosahedral clusters containing $\sim$600 Pd atoms, where 45% of these are located at the surface. According to X-ray photoelectron spectroscopy analysis, the Pd clusters exhibit an oxidized surface forming a PdO_x shell. Given the well-defined experimental system, as verified by electron microscopy data and theoretical simulations, we performed ab initio simulations using 10 functionalized graphenes (with vacancies or pyridine, amine, hydroxyl, carboxyl, or epoxy groups) to understand the adsorption process of BnSH, their further role in the Pd cluster formation, and the electronic properties of the graphene−nanoparticle hybrid system. Both the experimental and theoretical results suggest that Pd clusters interact with functionalized graphene by a sulfur bridge while the remaining Pd surface is oxidized. Our study is of significant importance for all work related to anchoring of nanoparticles on nanocarbon-based supports, which are used in a variety of applications.
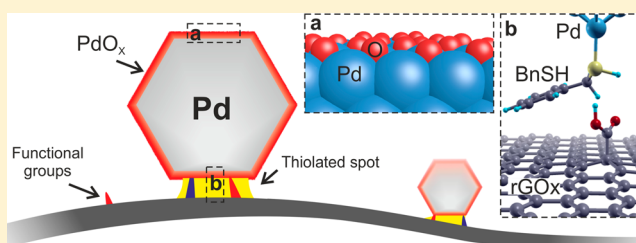
1. INTRODUCTION

Currently the generation of structural defects[1] and chemical functionalization[2,3] on graphene has been widely used as a mechanism to directly modify its electronic, mechanical, and chemical properties. These new properties will dictate how graphene interacts with its surroundings, promoting new chemical bonds, improving charge transfer, and altering the electron transport. Among graphene derivatives, reduced graphene oxide (rGOx) is widely used in diverse applications because of its simple preparation process that can be easily scaled-up. However, rGOx still contains a large number of defects and functional groups on its surface, especially if produced by chemical exfoliation followed by chemical reduction. Hence, it is important to understand the resulting electronic properties of defective and low-functionalized graphenes and how these materials interact with their surroundings.

During the last years, a large variety of inorganic nanostructures (e.g., metals, oxides, and chalcogenides) have been deposited on graphene and its derivatives.[4] Palladium−nanocarbon composites have attracted special attention because of the wide range of applications in biosensors,[5] fuel cells[6] and as catalysts for organic reactions.[7,8] These composites generally

show synergistic effects demonstrating good potential for real-life applications. Functionalized nanocarbons with thiol groups have been widely used as a support for metallic nanoparticles, where the main interactions arise from the sulfurated sites. Thiolated nanocarbons have shown enhanced interaction and larger binding sites for nanoparticles of noble metals such as Au[9] and Pt.[10] Moreover, the use of thiolated supports has been shown to improve the homogeneity and help to decrease the particle size of Pt clusters, where the composite also exhibited enhanced electrocatalytic activity for the oxygen reduction reaction (ORR).[10,11] Specifically, the attachment of benzyl mercaptan (BnSH) on carbon nanotubes affords an excellent binding material for Pt nanoparticles with a high density of thiol groups and a shorter distance between the nanoparticle and substrate.[12] However, despite numerous studies of graphene−nanoparticle composites, there is a clear lack of studies analyzing the interactions between the support and nanoparticles in well-defined systems where both experimental and theoretical data are reported. This lack of understanding hinders proper engineering of new nanomaterials for specific
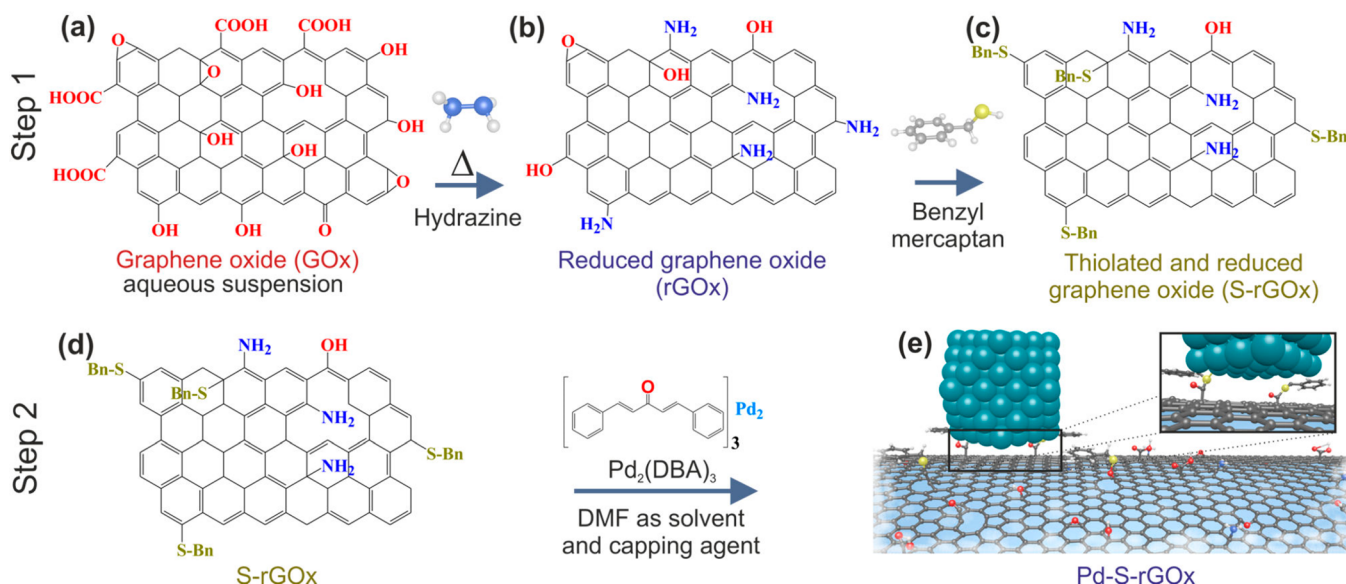
Figure 1. Pd−S-rGOx synthesis scheme. (a−c) Step 1 illustrates the preparation of thiolated and reduced graphene oxide (S-rGOx). (d, e) Step 2 exemplifies the synthesis of cuboctahedral and icosahedral Pd clusters on S-rGOx.

applications, since the interface strongly affects their final properties.

We present an experimental and theoretical study of a palladium-decorated reduced graphene oxide (Pd−S-rGOx) composite. Through a simple and fast method, we were able to anchor six-shell Pd-clusters with narrow and well-defined diameter (2.3 ± 0.3 nm). The Pd clusters were shaped as cuboctahedral or icosahedral single crystals containing ~600 Pd atoms, 45% of which were located at the surface. Interestingly, the size of the six-shell structures exactly corresponds with the size at which the energetic stabilities of cuboctahedral and icosahedral geometries match, explaining our experimental observation of both structures by high-resolution microscopy. By X-ray photoelectron spectroscopy (XPS) analysis we identified different chemical species present in the samples, and by complementing our studies with ab initio calculations we gained insight into the electronic properties, the adsorption mechanism, and the charge transfer in all the involved steps of the adsorption processes. Our experimental and theoretical results strongly suggest that the Pd clusters interact with functionalized graphene by sulfur-containing functional groups while the remaining Pd surface is oxidized.

2. EXPERIMENTAL AND COMPUTATIONAL DETAILS

Synthesis of S-rGOx. Graphene oxide was produced by a modified Hummer method[13,14] using natural flake graphite (Alfa Aesar Corporation, 99.9999%) as the starting material. rGOx was synthesized as follows:[15] 50 mg of graphene oxide was mixed in 75 mL of deionized water and sonicated for 1 h, and then the suspension was heated to 100 °C in an oil bath; 60 μL of hydrazine (Merck, 80% in water) was then added, the temperature was maintained for another 1 h. After the reduction process was finished, 13 mL of ethanol containing 1 mL of BnSH (Aldrich, 99%) was added to the rGOx solution, and the resulting mixture was stirred for 10 min. Finally, the obtained suspension was cooled to room temperature, and the resulting material (labeled as S-rGOx) was washed using acetone and ethanol several times. The synthesis scheme is depicted in Figure 1a−c.

Decoration Process. An 8.4 mg sample of S-rGOx was mixed with 9.4 mg of tris(dibenzylideneacetone)dipalladium(0), $Pd_2(DBA)_3$ (Sigma-Aldrich, 97%) in 25 mL of anhydrous N,N-dimethylformamide

(DMF) (Sigma-Aldrich, 99.8%) and ultrasonicated for 20 min, and then the suspension is stirred overnight. The resulting Pd-decorated graphene (Pd−S-rGOx) was centrifuged and dried in a vacuum oven. All of the chemicals were used as received without further purification. Figure 1d,e illustrates the synthesis process.

Material Characterization. The synthesized samples were characterized by XPS using a Kratos Axis Ultra DLD electron spectrometer equipped with a monochromatized Al Kα source operated at 150 W. Transmission electron microscopy (TEM) was carried out on a JEOL 1230 transmission electron microscope at 80 keV. Thermogravimetric analysis (TGA) was performed on a Mettler Toledo TGA/DSC 1 LF/948 instrument at a heating rate of 5 °C/min up to 1000 °C in pure oxygen. X-ray diffraction was carried out on a Siemens D5000 diffractometer with Cu Kα radiation (λ = 1.5418 Å) and an accelerating voltage of 40 kV.

Theoretical Calculations. We used density functional theory (DFT) within the local density approximation[16] using the Ceperley−Alder[17] parametrization implemented in the SIESTA code.[18] The wave functions for the valence electrons were represented by a linear combination of pseudoatomic numerical orbitals[19] using a double-ζ basis for H, C, N, and O, while a double-ζ plus polarization orbital was used for S and Pd. The real-space grid used for charge and potential integration was equivalent to a plane-wave cutoff energy of 250 Ry. The systems were constructed using a two-dimensional (2D) square graphene supercell (GS) (~2.5 nm × 2.5 nm) containing 240 atoms. Ten different defects were introduced at the center of the graphene supercell: (1) a vacancy (Vc); (2) substitutional nitrogen (N_{sub}); (3) Vc with pyridinic N (Vc-N); (4) amine ($R-NH_2$); (5) vacancy + amine ($Vc-NH_2$); (6) hydroxyl (R-OH); (7) vacancy + hydroxyl (Vc_2-OH); (8) carboxyl (R-COOH); (9) vacancy + hydroxyl (Vc-OH); and (10) epoxy. Nonmodified graphene (11) was also considered. In the above, Vc- and Vc_2- indicate that one or two vacancies were generated on the graphene surface before the addition of the functionality, while R- indicates that the functional group was directly attached to graphene without vacancies. Periodic boundary conditions were used, and the intergraphene distance was kept to a minimum of 60 Å to avoid interactions. Sampling of the 2D Brillouin zone was carried out with a 1 × 5 × 5 Monkhorst−Pack grid,[20] but the density of states was obtained using a 1 × 16 × 16 grid. Because of the 2D periodicity of the system, both the total energy and atomic forces were corrected by a self-consistent dipole correction. All of the systems were relaxed by conjugate gradient minimization until the maximum force was <0.05 eV/Å.

Adsorption Process. The adsorption process was separated into two steps: (1) First, one molecule of BnSH was placed above the nondefective surface or near the functionality on modified surfaces, and then the system was geometrically optimized. These systems are labeled BnSH-GS. (2) For the second adsorption process, the BnSH-GS systems were used as adsorbents. In each case, an icosahedral cluster containing 13 atoms of palladium (Pd_{13}) was placed above the thiol group from the BnSH molecule, and then the whole system was geometrically optimized. In both processes, the adsorption energy (ΔE_{ads}) was calculated. This is defined as $\Delta E_{ads} = E_{total} - E_{surf} - E_{mol}$, where E_{total} is the energy of the total system (adsorbent + adsorbate), E_{surf} is the energy of the adsorbent (i.e., modified GS or BnSH-GS system), and E_{mol} is the energy of the adsorbate (i.e., isolated BnSH or Pd_{13} cluster).

Charge Transfer Analysis and TEM Imaging Simulation. Bader analysis[21,22] was performed using the optimized geometries of the BnSH-GS systems. In order to quantitatively compare the transferred charge among constituents we used 300 Ry as the energy cutoff for the real-space grid during the DFT calculations. Simulations of TEM images were performed by using the multislice approach as described by Gómez-Rodríguez et al.[23]

3. RESULTS AND DISCUSSION

The process for synthesizing thiolated graphene oxide decorated with palladium clusters (Pd–S-rGOx) is illustrated in Figure 1. As described in Experimental and Computational Details, we first prepared a suitable substrate (S-rGOx) to achieve numerous anchoring sites in order to obtain homogeneous coverage of small Pd clusters. The resulting composite was analyzed by TEM, and the results are depicted in Figure 2a. The Pd clusters are very well dispersed over the graphene surface, with no signs of agglomeration into larger particles. High-resolution TEM (HRTEM) studies revealed that the Pd clusters exhibit a crystalline structure and a homogeneous size distribution (Figure 2b) with an average particle size of 2.3 ± 0.3 nm (given by a Gaussian fit from HRTEM analysis of 230 randomly chosen Pd nanoparticles; see Figure S1 in the Supporting Information). Detailed analysis indicated that Pd clusters may exhibit a cuboctahedral structure, but we also observed Pd clusters with icosahedral geometry (Figure 2c–e). Cuboctahedral clusters belong to the symmetry group O_h and are directly built on the basis of a face-centered cubic (fcc) lattice. They exhibit eight triangular faces consisting of close-packed (111) crystal planes that minimize the surface energy and six square faces that reveal the (100) surface, which is less energetically favorable. On the other hand, icosahedral clusters belongs to the I_h symmetry group and can be obtained directly from the cuboctahedron after a Mackay transformation.[24] Both solids are shell structures, and interestingly, the six-shell O_h and I_h Pd clusters have average diameters of ~2.4 and ~2.3 nm, respectively, both of which match perfectly with the experimentally observed diameter (2.3 ± 0.3).

Simulations of various TEM images of a six-shell icosahedral cluster and a six-shell cuboctahedral cluster, both containing 561 atoms, and the corresponding molecular models are depicted in Figure 2c–e. The experimental TEM images of the nanoparticles in Figure 2c,d show the characteristic fivefold and twofold rotation axes of icosahedral clusters, which are in good agreement with the I_h-Pd_{561} molecular model and the simulated TEM images. Figure 2e shows a Pd nanoparticle that matches the O_h-Pd_{561} cluster viewed along one of its threefold rotation axes.

Stability studies for small Pd_N clusters using DFT[25,26] indicated that icosahedral structures are favored over both decahedral and cuboctahedral structures when N = 13, 55, and
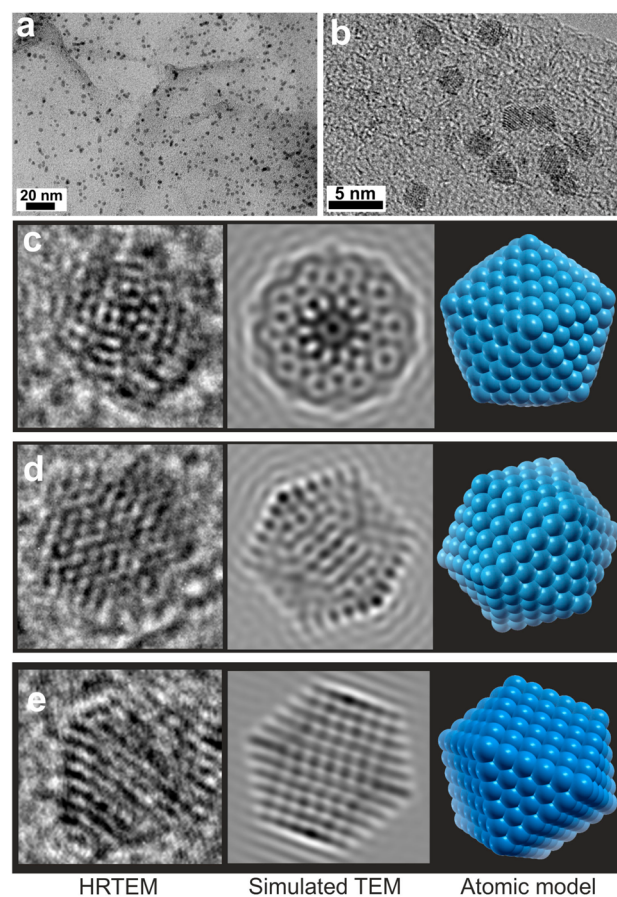
Figure 2. (a, b) TEM micrographs of well-dispersed and homogeneous 2.3 ± 0.3 nm Pd clusters on S-rGOx. (c, d) HRTEM micrographs, simulated TEM images, and molecular models of six-shell icosahedral clusters, where the (c) fivefold and (d) twofold symmetries are observed. (e) HRTEM micrograph, simulated TEM image, and molecular model of a six-shell cuboctahedral cluster.

147. The lowest-energy structure was found to be a slightly distorted icosahedron, and also, the existence of magnetic properties was suggested. Studies of larger Pd_N clusters by tight-binding calculations[27] reveal that the icosahedral structure is still lower in energy than the cuboctahedral one for Pd_{309} (five-shell) particles and similar in energy for Pd_{561} (six-shell) particles, while for Pd_{1415} (eight-shell) particles, the cuboctahedral structure becomes energetically favored. Furthermore, the activation energy for the Mackay transformation (transforming the icosahedral structure to the cuboctahedral structure) is around 12 to 45 meV for Pd_{55} to Pd_{309} clusters, respectively. Clearly, such low activation energies may explain the coexistence of the two geometries at intermediate sizes.

We also performed the Pd decoration directly on rGOx (without BnSH), and in agreement with previous studies,[28,29] we observed that the decoration process without BnSH results in larger Pd nanoparticles, and more importantly, the coverage and spatial distribution are not homogeneous (see Figure S2 in the Supporting Information). However, when thiolated substrates are used,[6,30] such as S-rGOx, the Pd nanoparticles exhibit smaller sizes, improved spatial distribution, and poor or null agglomeration because of the stronger interaction with the thiolated graphene surface. This suggests that when S-rGOx is used as the substrate, new specific sites exist where Pd strongly interacts with the S-rGOx and nucleates into nanoparticles
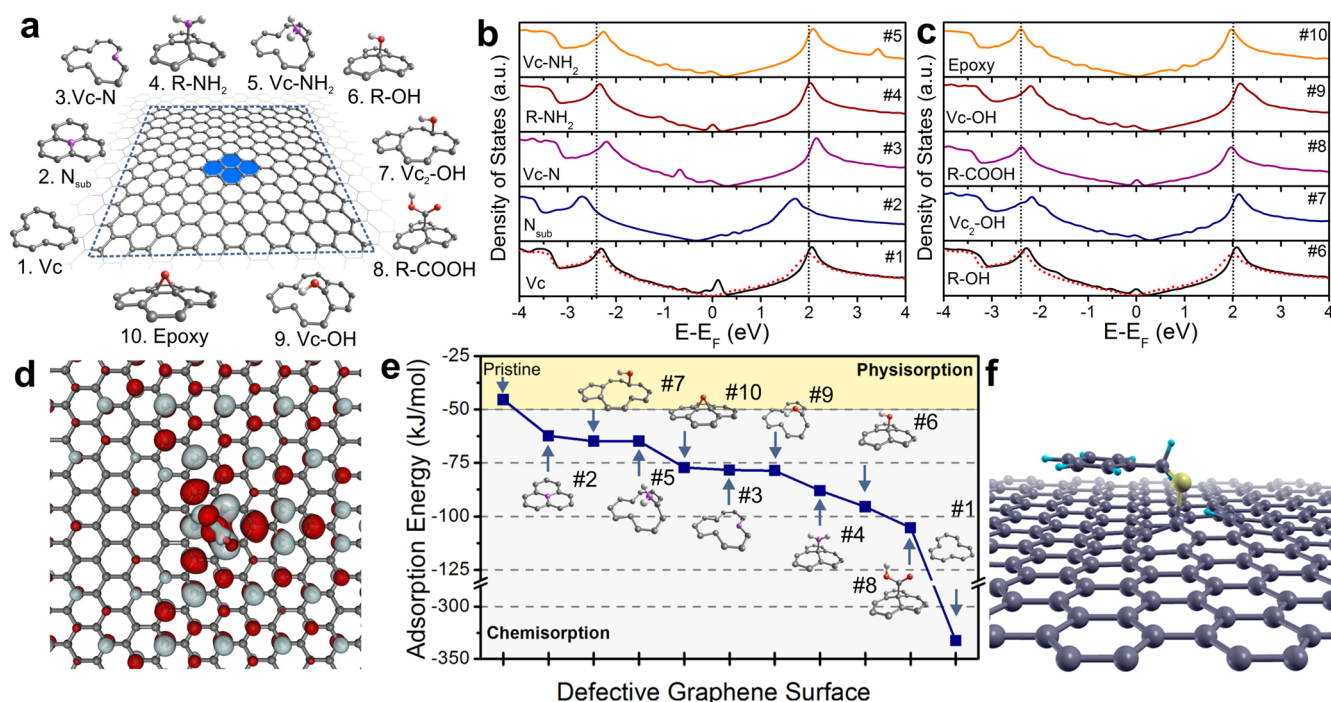
Figure 3. (a) The 10 defects and functional groups introduced on the graphene surfaces, as explained in main text. The blue area indicates the place where the defects are introduced, and the dashed line indicates the 2D supercell. (b, c) DOS of modified graphene surfaces. The numbers indicate the defects shown in (a). (d) Isosurface wave function of the new states introduced by the R-COOH functionality (defect #8), plotted at 0.03 e Å^{-3}. (e) Adsorption energy (ΔE_{ads}) of benzyl mercaptan (BnSH) on pristine and modified graphene. (f) Optimized geometry of BnSH chemisorbed on a vacancy (defect #1).

passivated by DMF. We point out that during the preparation of S-rGOx, the material was washed with ethanol and acetone, both of which are excellent solvents for BnSH, and we therefore expect the remaining BnSH, after the washing process, to be strongly attached (chemisorbed) to diverse defects and functionalities on the rGOx. This explains the strong binding of Pd nanoparticles with graphene through thiolated spots. To investigate our hypothesis, we studied the adsorption events and chemical reactions using DFT.

3.1. Electronic Properties of Functionalized Graphene. The decoration process was studied by dividing it into two adsorption events, where the first one is the chemisorption of BnSH on graphene and the second is adsorption of the Pd cluster on BnSH-GS.

Here we selected 10 functionalities (1) a vacancy (Vc); (2) substitutional nitrogen (N_{sub}); (3) Vc with pyridinic N (Vc-N); (4) amine (R-NH$_2$); (5) vacancy + amine (Vc-NH$_2$); (6) hydroxyl (R-OH); (7) vacancy + hydroxyl (Vc$_2$-OH); (8) carboxyl (R-COOH); (9) vacancy + hydroxyl (Vc-OH); and (10) epoxy. The functionalities were selected on the basis of our XPS analysis (discussed below) together with common defects that are known to form in rGOx.[31,32] The adsorption process was compared with that on nonmodified graphene. Figure 3a shows the 2D graphene supercell used during the DFT calculations together with the introduced defects and functional groups. The modified surfaces exhibit different electronic properties, as shown by the densities of states (DOS) plotted in Figure 3b,c. First, we note that there are three isolated cases. The Vc system (defect #1 in Figure 3a) exhibits highly localized states on the Fermi level (FL) due the unpaired electron of one C atom next to the vacancy. In the case of substitutional nitrogen (#2), the FL is shifted to the conduction band (exhibiting n-type doping), and no localized states are

observed. The last is the epoxy defect (#10), which introduces new states in the conduction band and opens a small band gap.

The rest of the modified graphene surfaces display a clear tendency in the electronic properties, where all of the surface functionalizations that partially modify the sp^2 hybridization of carbon atoms, such as R-NH$_2$ (#4), R-OH (#6), and R-COOH (#8), induce an impurity state near the FL, as observed in Figure 3b,c. Similar results have been observed for single-walled carbon nanotubes (SWCNTs).[33−35] The isosurface wave functions of these new states indicate that they are mainly positioned on the functional groups, as illustrated for defect #8 in Figure 3d. These localized states act as strong scattering sites for electron transport, a characteristic that is not desirable in electronics and is probably disadvantageous in catalytic applications as well. The modified surfaces containing one or two vacancies accompanied by functional groups [Vc-N (#3), Vc-NH$_2$ (#5), Vc$_2$-OH (#7), and Vc-OH (#9)] show a shift of the FL to the valence bands, thus exhibiting p-type doping and less pronounced state localization. Similar effects have been observed for SWCNTs, where one or two vacancies generate p-type doping.[36] Most functional groups on graphene are excellent adsorbent materials[33] and act as potential binding sites for nanoparticles and chemical reactions.[37,38]

3.2. Adsorption of Benzyl Mercaptan. Until here, we have analyzed the properties of functionalized graphene. However, it is essential to understand how feasible and strong the interaction between these defects and BnSH might be. To evaluate their interaction capabilities, we determined the adsorption energies (ΔE_{ads}) of benzyl mercaptan, which are displayed in Figure 3e. We observe strong interactions of BnSH with the defective surfaces, while pristine graphene exhibits $\Delta E_{ads} = -45.5$ kJ/mol, which can be classified as physisorption ($|\Delta E_{ads}| < 50$ kJ/mol). Such a low interaction energy agrees

6629

dx.doi.org/10.1021/ja412259h | J. Am. Chem. Soc. 2014, 136, 6626–6633

with that of benzene derivatives adsorbed on nonmodified carbon nanotubes.[12] A simple addition of one substitutional nitrogen (N_{sub}, defect #2) increases ΔE_{ads} to −62.4 kJ/mol, which although rather weak can be classified as chemisorption. Actually, seven out of the 10 defective surfaces exhibit adsorption energies higher than −70 kJ/mol for the BnSH molecule. Except for Vc (defect #1), which because of the unpaired electron can form a direct covalent bond between the S atom and the graphene and thus exhibits the highest adsorption energy (−332.6 kJ/mol), the functional groups R-NH_2 (#4), R-OH (#6), and R-COOH (#8) exhibit the highest adsorption energies, around double as high as for the pristine surface. The main interaction for aromatic compounds on pristine graphene is $\pi-\pi$ stacking, which proceeds with negligible charge transfer,[12] while functionalized surfaces interact with the BnSH molecules mainly through their functional groups. Here, the electronegativity of the functional group plays a key role, since the main contact is performed by hydrogen bonding, and the benzene ring has only an indirect effect on the adsorption.[12] In Figure 3f we show the optimized geometry for Vc (defect #1), but the optimized geometries of all systems are depicted in Figure S3 in the Supporting Information. In Table 1 we list the values of the adsorption energies for all defects.

Table 1. Distance between the Thiol Group and Defective Graphene, Adsorption Energy and Charge Transfer of BnSH, and Adsorption Energy of the Pd$_{13}$ Cluster

defect	SH−defect (Å)[a]	BnSH ΔE_{ads} (kJ/mol)	Bader charge (e$^-$)[b]	Pd$_{13}$ ΔE_{ads} (kJ/mol)
1	1.09	−332.55	−0.415	−119.26
2	3.06	−62.37	0.001	−181.13
3	1.74	−78.38	0.027	−279.97
4	1.65	−87.98	0.048	−322.24
5	1.87	−64.81	0.021	−149.21
6	1.70	−95.54	−0.023	−294.05
7	1.80	−64.81	−0.021	−171.41
8	2.68	−105.36	−0.141	−150.28
9	2.08	−78.59	−0.017	−224.83
10	1.72	−77.21	−0.023	−172.50
11	2.43	−45.47	0.030	−161.03

[a]Distance between thiol group in BnSH and the graphene surface. [b]Negative Bader charge indicates electron transfer from the BnSH molecule to the graphene substrate.

The Bader charge[21,22] measures the charge transfer between the defective graphene surface and the adsorbed BnSH molecule. We list these values in Table 1 and note that all of the graphenes containing oxygenated functional groups exhibit an increase in electronic charge after BnSH adsorption. On the other hand, pristine graphene, N-doped graphene, and nitrogenated functional groups exhibit positive Bader charges, indicating charge transfer from the defective graphene to the BnSH molecule. In line with expectations, the magnitudes of the Bader charge qualitatively agree with the trend in ΔE_{ads} in Figure 3e.

It is also important to know that sulfur compounds (hydrogen sulfide, thiols, thiolate anions RS$^-$, etc.) are Lewis bases, and because of the relatively weak S−H bond in thiols, we already expect the formation of thiolate anions. Since these are strong nucleophiles, they may further react with some functional groups present on rGOx. The trend in the

adsorption energies (Figure 3e) is indicative of the chemical reactivity of modified surfaces and can be well-correlated with the electronic properties of functionalized graphene. As shown in Figure 3c,d, the systems with highly localized states near the FL also exhibit the highest adsorption energies, while those with less pronounced state localization show lower ΔE_{ads}. It is worthwhile to mention that studies of chemical reactions in solution by DFT are certainly a challenge, since the solvent effects are not included during the simulations. However, as previously shown, trends in the adsorption energy can successfully be used to describe adsorption events and chemical reactions in diverse systems.[12,33,38,39]

As we previously mentioned, most adsorption events are strong enough to be considered as chemisorption. However, we did not observe a chemical bond between the BnSH molecule and the modified graphene surfaces. This can be attributed to the presence of an energy barrier that characterizes most chemical reactions. This characteristic is not naturally observed during geometrical optimization because of the low thermal energy to overcome the barrier. In this sense, we complemented the DFT computations by studying the composite with BnSH already attached to the graphene substrate. After the computation of the reaction energy (see Table S2 and Figure S4 in the Supporting Information), we found that surfaces with vacancies (#1, #3, #5, #7, and #9) and large functional groups (#8) are excellent candidates for the chemisorption of the BnSH molecule, preferring BnSH chemically bonded to rGOx. However, systems with small functional groups and no vacancies (pristine, #2, #4, #6, and #10) do not explicitly attach the BnS$^-$, most probably because of the planarity of the graphene surface and the steric repulsion with the benzyl group. However, the reaction energy is still negative, indicating the possibility of the reaction to proceed.
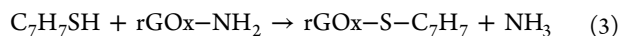
3.3. Adsorption of Pd$_{13}$ Cluster on BnSH-GSs. So far, we have analyzed the capabilities of BnSH to chemisorb on some specific defects and functional groups on rGOx, and now, we continue by studying the second adsorption process illustrated in Figure 1d,e. In this case, we used an icosahedral Pd$_{13}$ cluster (for such small systems the icosahedral geometry is preferred over the cuboctahedral) to simulate the Pd addition. All of the BnSH-GS systems offer good accessibility (Figure S3 in the Supporting Information), which significantly improves the Pd interaction compared with pristine or N-doped graphene surfaces.[40,41] Figure 4 displays the values of ΔE_{ads} for the
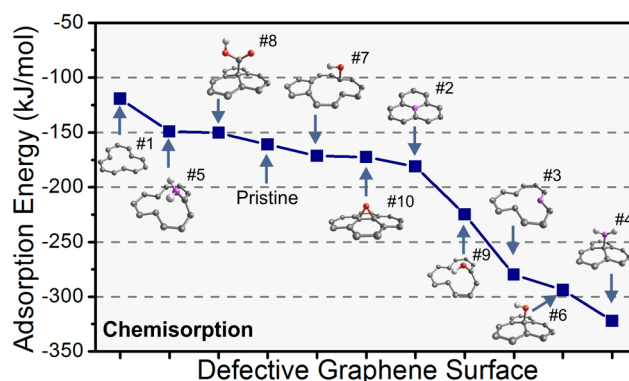
Figure 4. Adsorption energies (ΔE_{ads}) of the Pd$_{13}$ cluster on pristine and modified graphene surfaces. Chemisorption of the Pd$_{13}$ cluster through the BnSH molecule is observed, and the introduction of functionalities or defects substantially increases ΔE_{ads}.

Pd_{13} cluster on the BnSH-GS systems. We can notice the high adsorption energies ($|\Delta E_{ads}| > 100$ kJ/mol in all cases), indicating strong chemisorption. We also observed that the benzyl ring from BnSH does not limit the chemical reaction since the Pd−S bond is long (∼2.26 Å) and strong enough to overcome the steric repulsion. The relaxed structures are depicted in Figure S5 in the Supporting Information. We observe that the Pd_{13} cluster is always chemically bonded to the BnSH molecule, but we note that in this case the chemical bond is formed not with the defective graphene but between the Pd_{13} cluster and the BnSH complex.

This is explained by the fact that the DFT computations are performed in the gas-phase environment. However, in solvated systems the BnSH would most likely form a thiolate, which would increase the reactivity and result in a thiol bridge between palladium and graphene, as also discussed in the previous section. During the theoretical studies we observed the following chemical reactions:

$$C_7H_7SH + rGOx\text{-}Vc \rightarrow rGOx-H-S-C_7H_7 \qquad (1)$$

$$C_7H_7SH + rGOx-OH \rightarrow rGOx-S-C_7H_7 + H_2O \qquad (2)$$

$$C_7H_7SH + rGOx-NH_2 \rightarrow rGOx-S-C_7H_7 + NH_3 \qquad (3)$$

The chemical reaction shown in eq 1 was observed during the first adsorption event, while the chemical reactions in eqs 2 and 3 were not observed until Pd_{13} adsorption, where the Pd cluster catalyzes the reaction and the deposition process. Because of our model's simplicity, we did not observe the attachment of sulfur to the graphene; however, in real systems we may expect that the reactions in eqs 2 and 3 lead to the Pd−S−rGOx complex, as supported by the experimental observations. It is interesting that in this scheme, the reactions in eqs 2 and 3 produce subproducts that signify loss of oxygen and nitrogen from rGOx, in good agreement with the XPS experimental results. A summary of the elemental compositions in the different samples as measured by XPS is presented in Table S2 in the Supporting Information. It shows that the sulfur content in the S-rGOx sample (1.62%), assigned to anchored BnSH molecules, corresponds very well to the total decrease in nitrogen and oxygen content of the S-rGOx compared to the rGOx sample (0.17% + 1.50% = 1.67%). This strongly suggests that nitrogenated and in particular oxygenated groups are mainly responsible for BnSH interactions, as observed by DFT calculations.

3.4. XPS Analysis of the Pd−S-rGOx Composite. From our theoretical calculations, we have concluded that benzyl mercaptan plays a key role in the adsorption process by acting as a bridge between the metal nanoparticle and the defective graphene, thereby improving the anchoring efficiency and decreasing the particle size. Now, we complement our studies by further analysis of the Pd−S-rGOx samples to test our hypothesis. The processing of the XPS spectra (Shirley background subtraction, spectral component fitting, and quantification) was accomplished by Vision2 software (Kratos Analytical Ltd.). Chemical states of the elements were assigned using the National Institute of Standards and Technology (NIST) database.[42] Figure 5 depicts the high-resolution spectra of C 1s, N 1s, S 2p, and Pd 3d photoelectron lines of the Pd−S-rGOx composite. The presence of all these elements is also supported by energy-dispersive X-ray spectroscopy (EDX) data (Figure S8 in the Supporting Information). The carbon spectrum, fitted by five Gaussian/Lorentzian (70/30) peaks,
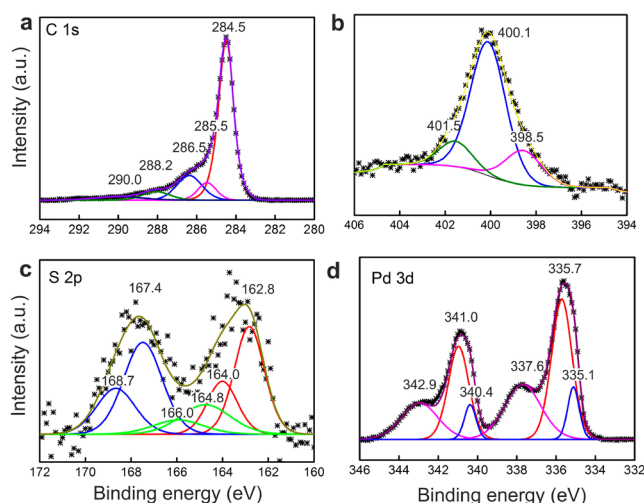
Figure 5. High-resolution XPS analysis of the Pd−S-rGOx composite: (a) C 1s; (b) N 1s; (c) S 2p, where the sulfur spectrum indicates the interaction of thiol groups with Pd clusters; (d) Pd 3d, which is observed to have a substantial contribution of PdO and less abundant metallic Pd.

is shown in Figure 5a. The shape of the spectrum and the position of the main peak at 284.5 eV are typical for sp^2-hybridized C of graphitic materials, while the defective regions containing C−O bonds partly contribute to the 285.5 and 286.5 eV peaks. The component at 286.5 eV can also include C−N and C−SH bonds, while the fitted peaks at higher energies were used to fit the vibrational structure of the C 1s spectrum, including $\pi-\pi^*$ excitation at 290.0 eV. The described spectral structure is typical in nanostructured carbon systems. The N spectrum, shown in Figure 5b, displays two strong signals at 400.1 and 398.5 eV, matching pyrrole-type N and amine R-NH_2 in carbon samples, which can be rationalized by the use of DMF or hydrazine in the reduction process. The third N 1s component at 401.5 eV seems to be related to protonated amine groups. The XPS data therefore are consistent with the theoretical models used during DFT computations by confirming the presence of diverse functional groups, such as #3, #5, and #8, in our S-rGOx sample.

The XPS S 2p spectrum (Figure 5c) shows three doublets. The low-binding-energy doublet (S $2p_{3/2}$ at 162.8 eV and S $2p_{1/2}$ at 164.0 eV) is assigned to the sulfur in BnSH. The S $2p_{3/2}$ binding energy is shifted by 0.4 eV to lower values relative to the sulfur in S-rGOx (Figure S7 in the Supporting Information), indicating the interaction of the thiol molecules with the Pd clusters. The weak S 2p doublet at 164.8 and 166.0 eV could be assigned to the sulfur in protonated or/and partially oxidized thiol groups, while the high-binding-energy S 2p doublet at 167.4 and 168.7 eV is attributed to sulfonyl (S−O) and/or sulfate (S═O) groups generated during the graphite oxidation process. From Table S2 in the Supporting Information it appears as though the sulfur signal decreases significantly in the Pd−S-rGOx composite compared with S-rGOx. We believe that this is rationalized by the fact that most of these sulfur atoms take part in thiol bridges and therefore are "screened" by the above-lying Pd clusters. This observation therefore gives further support that the thiol bridges play an active role in the adsorption mechanism of the Pd clusters. We also point out that clear sulfur signals in the Pd−S-rGOx composite can be seen in the EDX spectrum (Figure S8 in the Supporting Information). Figure 5d shows the Pd spectrum,

which comprises three doublet peaks. The first doublet (Pd $3d_{5/2}$ at 335.1 eV and Pd $3d_{3/2}$ at 340.4 eV) corresponds to metallic Pd. The other two doublets (335.7 and 341.0 eV and 337.6 and 342.9 eV) can be rationalized by a PdO core−shell structure with a saturated Pd oxide shell (Pd $3d_{5/2}$, 337.6 eV) at the surface and a Pd−PdO interfacial layer at the core, which is depleted in oxygen. The structure can be explained both by surface passivation by DMF and high reactivity toward oxygenation due to their very small size (which might occur also in the time between their synthesis and the XPS measurements). Overall, our XPS data suggest that Pd nanoparticles interact with the rGOx surface via thiol bridges and that they are in reality Pd−PdO$_x$ core−shell nanoparticles.

This is in line with expectations due to the higher oxygen affinity that Pd nanoparticles exhibit, showing a tendency to oxidize in order to decrease the surface energy.[39] Similar results have been observed in our previous publications.[6,30]

3.5. Description of Pd−PdO$_x$ Nanoparticles on S-rGOx. We have concluded that sulfur plays a key role in the strong interaction of Pd clusters with rGOx and that Pd−PdO$_x$ nanoparticles are consistent with six-shell cuboctahedral and icosahedral particles with 45% of the atoms located at the oxidized surface. Now, in order to complement the information, we analyzed the interface of the nanocomposite by considering the projected area of a 2.3 nm Pd sphere ($\sim$4.15 nm^2). Within this surface area, graphene exhibits $\sim$170 carbon atoms. Our experimental characterization indicates that S-rGOx contains 1.62% sulfur, which arises directly from the chemisorbed BnSH (Table S1 and Figure S7 in the Supporting Information). This suggests that under a single Pd nanoparticle, we may expect at least three thiols binding the graphene and Pd cluster together. This value sets a lower limit on the number of thiols that might be involved in the PdO$_x$−BnSH−rGOx bonding. However, this assumption considers a homogeneous distribution of thiols along the graphene surface. It is highly possible that some defective areas in the graphene might lead to a more dense agglomeration of thiols, so we point out that our estimation sets a lower limit on the number of thiol molecules that act as binding sites to each Pd cluster.

4. CONCLUSIONS

We have analyzed the interface of palladium nanoparticles and reduced graphene oxide by means of density functional theory and X-ray photoelectron spectroscopy. We found that benzyl mercaptan strongly interacts, via its thiol group, with defects and functionalities present in the rGOx and later acts as a strong anchoring site for Pd nanoparticles. The as-synthesized Pd clusters exhibit a six-shell cuboctahedral or icosahedral geometry, and because of their large surface area, these Pd clusters are partly oxidized at the surfaces, exhibiting a Pd−PdO$_x$ core−shell structure. We have described in detail the interaction at the interface of the Pd−S-rGOx composite in regard to the formation of chemical bonds, the electronic charge transfer, and the electronic properties of the reduced graphene surface. Our study will be of significance for all studies related to composites of metallic nanoparticles on carbon supports, a field that has an impact on both scientific and engineering research.

ASSOCIATED CONTENT

Ⓢ Supporting Information
TEM, XPS, and EDX data; particle size histogram of Pd nanoparticles on S-rGOx; and DFT-optimized structures of adsorbed Pd$_{13}$ and BnSH on GSs. This material is available free of charge via the Internet at http://pubs.acs.org.

AUTHOR INFORMATION

Corresponding Author
thomas.wagberg@physics.umu.se

Author Contributions
§E.G.-E. and G.H. contributed equally.

Notes
The authors declare no competing financial interest.

REFERENCES

(1) Banhart, F.; Kotakoski, J.; Krasheninnikov, A. V. *ACS Nano* **2011**, *5*, 26−41.
(2) Sun, Z.; James, D. K.; Tour, J. M. *J. Phys. Chem. Lett.* **2011**, *2*, 2425−2432.
(3) Dreyer, D. R.; Park, S.; Bielawski, C. W.; Ruoff, R. S. *Chem. Soc. Rev.* **2010**, *39*, 228−240.
(4) Huang, X.; Qi, X.; Boey, F.; Zhang, H. *Chem. Soc. Rev.* **2012**, *41*, 666−686.
(5) Lu, L.-M.; Li, H.-B.; Qu, F.; Zhang, X.-B.; Shen, G.-L.; Yu, R.-Q. *Biosens. Bioelectron.* **2011**, *26*, 3500−3504.
(6) Hu, G.; Nitze, F.; Barzegar, H. R.; Sharifi, T.; Mikołajczuk, A.; Tai, C.-W.; Borodzinski, A.; Wågberg, T. *J. Power Sources* **2012**, *209*, 236−242.
(7) Li, Y.; Fan, X.; Qi, J.; Ji, J.; Wang, S.; Zhang, G.; Zhang, F. *Nano Res.* **2010**, *3*, 429−437.
(8) Scheuermann, G. M.; Rumi, L.; Steurer, P.; Bannwarth, W.; Mulhaupt, R. *J. Am. Chem. Soc.* **2009**, *131*, 8262−8270.
(9) Hu, J.; Shi, J.; Li, S.; Qin, Y.; Guo, Z.-X.; Song, Y.; Zhu, D. *Chem. Phys. Lett.* **2005**, *401*, 352−356.
(10) Kim, Y.-T.; Mitani, T. *J. Catal.* **2006**, *238*, 394−401.
(11) Yang, G.-W.; Gao, G.-Y.; Zhao, G.-Y.; Li, H.-L. *Carbon* **2007**, *45*, 3036−3041.
(12) Woods, L. M.; Bădescu, Ş. C.; Reinecke, T. L. *Phys. Rev. B* **2007**, *75*, No. 155415.
(13) Stankovich, S.; Piner, R. D.; Chen, X. Q.; Wu, N. Q.; Nguyen, S. T.; Ruoff, R. S. *J. Mater. Chem.* **2006**, *16*, 155−168.
(14) Hummers, W. S.; Offeman, R. E. *J. Am. Chem. Soc.* **1958**, *80*, 1339.
(15) Stankovich, S.; Dikin, D. A.; Piner, R. D.; Kohlhaas, K. A.; Kleinhammes, A.; Jia, Y.; Wu, Y.; Nguyen, S. T.; Ruoff, R. S. *Carbon* **2007**, *45*, 1558−1565.
(16) Kohn, W.; Sham, L. J. *Phys. Rev.* **1965**, *140*, A1133−A1138.
(17) Ceperley, D. M.; Alder, B. J. *Phys. Rev. Lett.* **1980**, *45*, 566−569.
(18) Soler, J. M.; Artacho, E.; Gale, J. D.; García, A.; Junquera, J.; Ordejón, P.; Sánchez-Portal, D. *J. Phys.: Condens. Matter* **2002**, *14*, 2745−2779.
(19) Junquera, J.; Paz, Ó.; Sánchez-Portal, D.; Artacho, E. *Phys. Rev. B* **2001**, *64*, No. 235111.
(20) Monkhorst, H. J.; Pack, J. D. *Phys. Rev. B* **1976**, *13*, 5188−5192.
(21) Tang, W.; Sanville, E.; Henkelman, G. *J. Phys.: Condens. Matter* **2009**, *21*, No. 084204.
(22) Sanville, E.; Kenny, S. D.; Smith, R.; Henkelman, G. *J. Comput. Chem.* **2007**, *28*, 899−908.

(23) Gómez-Rodríguez, A.; Beltrán-del-Río, L. M.; Herrera-Becerra, R. *Ultramicroscopy* **2010**, *110*, 95−104.

(24) Mackay, L. *Acta Crystallogr.* **1962**, *15*, 916−918.

(25) Zhang, W.; Ge, Q.; Wang, L. *J. Chem. Phys.* **2003**, *118*, 5793−5801.

(26) Kumar, V.; Kawazoe, Y. *Phys. Rev. B* **2002**, *66*, No. 144413.

(27) Barreteau, C.; Desjonqueres, M. C.; Spanjaard, D. *Eur. Phys. J. D* **2000**, *11*, 395−402.

(28) Nitze, F.; Mazurkiewicz, M.; Malolepszy, A.; Mikolajczuk, A.; Kędzierzawski, P.; Tai, C.-W.; Hu, G.; Kurzydłowski, K. J.; Stobinskib, L.; Borodzinskib, A.; Wågberg, T. *Electrochim. Acta* **2012**, *63*, 323−328.

(29) Hu, G. Z.; Nitze, F.; Jia, X.; Sharifi, T.; Barzegar, H. R.; Gracia-Espino, E.; Wagberg, T. *RSC Adv.* **2014**, *4*, 676−682.

(30) Hu, G.; Nitze, F.; Sharifi, T.; Barzegar, H. R.; Wågberg, T. *J. Mater. Chem.* **2012**, *22*, 8541−8548.

(31) Englert, J. M.; Dotzer, C.; Yang, G.; Schmid, M.; Papp, C.; Gottfried, J. M.; Steinrück, H.-P.; Spiecker, E.; Hauke, F.; Hirsch, A. *Nat. Chem.* **2011**, *3*, 279−286.

(32) Some, S.; Kim, Y.; Yoon, Y.; Yoo, H.; Lee, S.; Park, Y.; Lee, H. *Sci. Rep.* **2013**, *3*, No. 1929.

(33) Gracia-Espino, E.; López-Urías, F.; Terrones, H.; Terrones, M. Novel Nanocarbons for Adsorption. In *Novel Carbon Adsorbents*; Tascón, J. M. D., Ed.; Elsevier: Oxford, U.K., 2012; pp 3−35.

(34) Zhao, J. J.; Park, H. K.; Han, J.; Lu, J. P. *J. Phys. Chem. B* **2004**, *108*, 4227−4230.

(35) Park, H.; Zhao, J. J.; Lu, J. P. *Nano Lett.* **2006**, *6*, 916−919.

(36) Gracia-Espino, E.; Lopez-Urias, F.; Terrones, H.; Terrones, M. *Mater. Express* **2011**, *1*, 127−135.

(37) Georgakilas, V.; Otyepka, M.; Bourlinos, A. B.; Chandra, V.; Kim, N.; Kemp, K. C.; Hobza, P.; Zboril, R.; Kim, K. S. *Chem. Rev.* **2012**, *112*, 6156−6214.

(38) Wood, B. C.; Bhide, S. Y.; Dutta, D.; Kandagal, V. S.; Pathak, A. D.; Punnathanam, S. N.; Ayappa, K. G.; Narasimhan, S. *J. Chem. Phys.* **2012**, *137*, No. 054702.

(39) Zhang, L.; Henkelman, G. *J. Phys. Chem. C* **2012**, *116*, 20860−20865.

(40) Gracia-Espino, E.; Jia, X.; Wågberg, T. *J. Phys. Chem. C* **2014**, *118*, 2804−2811.

(41) Sharifi, T.; Gracia-Espino, E.; Barzegar, H. R.; Jia, X.; Nitze, F.; Hu, G.; Nordblad, P.; Tai, C.-W.; Wågberg, T. *Nat. Commun.* **2013**, *4*, 2319.

(42) *NIST X-ray Photoelectron Spectroscopy Database*, version 4.1; National Institute of Standards and Technology: Gaithersburg, MD, 2012; http://srdata.nist.gov/xps/.

6633

dx.doi.org/10.1021/ja412259h | *J. Am. Chem. Soc.* 2014, 136, 6626−6633